Weld Line Detection and Tracking via Spatial-Temporal Cascaded Hidden Markov Models and Cross Structured Light

Liguo Zhang, Qixiang Ye, *Member, IEEE*, Wei Yang, and Jianbin Jiao, *Member, IEEE*

***Abstract*— Unlike weld seam detection in a welding process, weld line localization for inspection is usually performed outdoors and challenged by noise and variation of illumination intensity. In this paper, we propose a weld line localization approach for mobile platform via a cross structured light (CSL) device and spatial-temporal cascaded hidden Markov models (HMMs). A CSL device is designed to project cross red laser stripes on weldment surfaces and capture the weld convexity in video sequences. Stripe edge images are extracted and then a spatial HMM is designed to detect the regions of interest (ROIs) in the video frames. Detected ROIs in successive video frames are fed to the proposed temporal HMM as observations to track the weld lines. In this way, we incorporate both the spatial characteristics of laser stripes and the continuity of the weld lines in an optimal framework. Experiments show that the proposed approach can effectively reduce the influence of illumination and noise, contributing a robust weld line detection and tracking system.**

***Index Terms*— Cross structured light (CSL), hidden Markov model (HMM), weld line detection, weld line tracking.**

I. Introduction

NONDESTRUCTIVE testing (NDT) of metal weldment is very important to guarantee the safety operation of lots of industry facilities, such as towers of the wind turbines and oil storage tanks. In automatic NDT systems, automatic weld line detection and tracking can navigate moving platforms and improve the testing performance and efficiency significantly.

Weld seam tracking in a welding process is the most relevant technique to weld line detection and tracking for inspection. Weld seam detection has a long research history and been one of the most successful automation techniques given the context that welding is performed indoors and the routes of platforms are planned. Different from weld seam tracking, weld line tracking is usually performed in the wild, with moving platforms, undetermined routes and unconstrained illumination. Therefore, the weld line tracking is more challenging than the former.

From the perspective of sensors, some approaches have been proposed for weld line detection, which include distance measurement [1], [2], vision-based approaches [3], [4], and structured light-based approaches [5], [6].

Distance measurement methods usually use distance sensor arrays to obtain accurate depth estimates of a row of points reflecting the convex shapes of the weld beads. However, since the depth estimates are usually discrete, it is difficult to describe the continuous nature of the weldment surface. In addition, depth information is invisible, which makes it difficult to operate the system in case manual intervention is required.

Vision-based approaches are more simple and intuitive than those based on distance sensor arrays. However, weld lines on painted surfaces often have a similar color to their background, which makes it difficult to discriminate the weld lines from the background. In addition, weld lines in the wild are often covered by dust, oil, and rust, which aggravate the difficulty.

In recent years, structured light-based approaches have attracted more and more attention in the measurement areas, such as automatic welding [7], [8], industry inspection [9]–[15], and robot navigation [16]–[20], because of its simplicity, noncontact, and strong anti-interference abilities. It is observed that most of the weld beads have small weld convexity formed in the welding process. Structured light is capable of capturing these convex shapes due to its capability of precise measurement.

When using the structured light in measurement, robust stripe extraction is the primary problem to be considered. Edge, color and center of stripe are the most used features for stripe extraction in the existing research [12]. With these features, Gaussian approximation [21], [22], center of mass [21], [22], linear approximation [21], [22], Blais and Rioux detectors [23], probability estimator [21], [22], finite-impulse response filter and first derivative [24], [25], spline interpolation [9], dynamic line models [26], and a line walking algorithm [27] have been proposed to extract stripes. Most of these existing approaches for laser stripe extraction are developed from the perspective of filtering or noise depression. However, a few of them consider the problem of long-duration variation of illumination intensity. In [8] and [28], Li *et al.* proposed to use temporal data association to filter out the

Manuscript received April 14, 2013; revised August 6, 2013; accepted August 7, 2013. Date of publication October 10, 2013; date of current version March 6, 2014. This work was supported in part by the National Basic Research Program of China (973 Program) under Grant 2011CB706900 and Grant 2010CB731800, and in part by the National Science Foundation of China under Grant 61039003, Grant 61271433, and Grant 61202323. The Associate Editor coordinating the review process was Dr. George Xiao.

L. Zhang, W. Yang, and J. Jiao are with the School of Electronics, Electrical and Communication Engineering, University of Chinese Academy of Sciences, Beijing 100029, China (e-mail: zhangliguo08@mails.ucas.ac.cn; jiaojb@ucas.ac.cn).

Q. Ye is with the School of Electronics, Electrical and Communication Engineering, University of Chinese Academy of Sciences, Beijing 100029, China, and also with the University of Maryland, College Park, MD 20740 USA (e-mail: qxye@ucas.ac.cn).

Color versions of one or more of the figures in this paper are available online at http://ieeexplore.ieee.org.

Digital Object Identifier 10.1109/TIM.2013.2283139

0018-9456 © 2013 IEEE. Personal use is permitted, but republication/redistribution requires IEEE permission.
See http://www.ieee.org/publications_standards/publications/rights/index.html for more information.

illumination noise from arc lights or splashes and detect stripes in video sequences. However, it is difficult to extend this approach to weld line detection because illumination variation in the wild is quite different from arc lights or splashes.

After the stripe extraction, it is required to localize the weld lines in video frames. In [5], Wang *et al.* use corner points (the intersection points between a laser stripe and a weld bead) to localize the points corresponding to both weld toes. Corner points from multiple frames are connected into lines using a Hough transform. It is known that Hough transform is widely applied to weld seam tracking in welding processes [29], [30]; however, it might not work well under the arbitrary motion of platforms and cross weld lines in NDT systems.

In this paper, we propose a spatial-temporal cascaded hidden Markov models (STC-HMMs) based approach for robust weld line detection and tracking on a moving platform working in the wild environment. The problem of the stripe extraction is formulated in a spatial HMM (S-HMM) framework, in which edge features are used as the observation and color features together with pixel locations are used to calculate the transition probability. On the extracted stripe, a measurement function of area, color and stripe width is defined to localize weld line regions of interest (ROIs) in each frame. To filter out random noise, located ROIs in video frames are fed to a designed temporal HMM (T-HMM) for filtering and tracking, with defined observations and transition probability on stripe locations, width and color similarity. The proposed STC-HMMs incorporate both the spatial and temporal characteristics of weld line stripes in an optimal framework, which can greatly improve the robustness to noise, illumination and platform motion.

Wall climbing robots are widely applied to NDT of metal facilities and recent research has made significant progress [31]–[34]. On the moving platform, both weld lines and their background are changing. HMM parameters estimated by Baum–Welch algorithm cannot adapt to the changing well. We propose a new parameter estimation strategy and then use the Viterbi decoding to find the optimal solutions.

Our approach is relevant to [9] and [10]. In [9], Usamentiaga *et al.* propose a split-remove-fill procedure to fit laser stripes, reduce noise, and fill gaps. In our system, since the convexity is very small, it is difficult to use a fitting procedure to discriminate the convex shape from noise. In [10], an elegant solution with uncertainty propagation to surface shape measurement is demonstrated. Our approach is different from the existing works on both the methodology and implementation details. First, our approach pursues optimal solutions by STC-HMMs but Molleda *et al.* [10] using a Monte Carlo algorithm. Second, our system is designed for weld line tracking while the work in [10] is designed for shape measurement of steel surfaces. In our system, laser stripes and weld lines are spatial-temporal continuous signals, and thus can be regarded as a stochastic process of observation sequence (such as color, location and shape), respectively. The underlying assumption of the HMMs is that the vision signals of weld lines in spatial and temporal domains can be well characterized as a parametric double-stochastic process. In addition, the parameters of the stochastic processes can be determined in a well-defined manner.

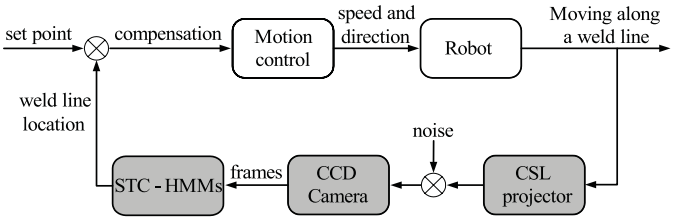

Fig. 1. Framework of the robot-based inspection platform. The measurement module is composed of a CSL projector, a CCD camera and weld line detection and tracking algorithms, which are all marked gray.

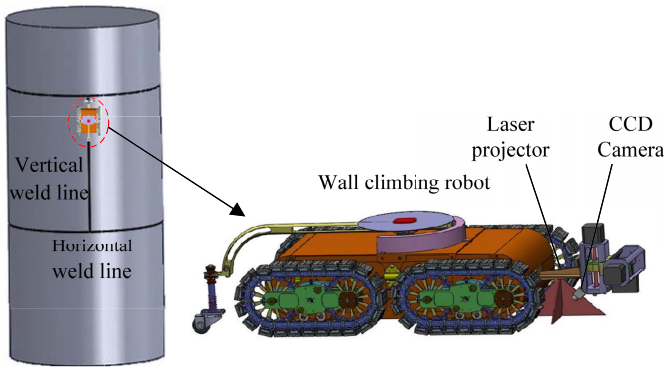

Fig. 2. Illustration of the platform composed of a climbing robot, an NDT system and a CSL device.

The remainder of this paper is organized as follows. A brief introduction of the cross structured light (CSL) platform on a robot platform is presented in Section II. The detail of the proposed weld line detection and tracking approach is described in Section III. The experiments are presented in Section IV and this paper is concluded in Section V.

II. Weld Line Inspection Platform

As shown in Figs. 1 and 2, the platform is composed of three modules: a moving module on a wall climbing robot, a NDT system, and a measurement module. The measurement module is composed of both hardware and software. The hardware includes a laser projector and a charge-coupled device (CCD) camera and the software is the tracking algorithms of STC-HMMs, as shown in Fig. 1. In practical operations, the robot moves along the weld lines under the control of the automatic information feedback from the measurement module.

As shown in Fig. 3, the CSL device is made up of a cross laser projector and a CCD camera. The laser projector is fixed perpendicularly to the weldment surface, while there is a 45° angle between the optical axis of the camera and the projector. The projector projects two orthogonal light planes onto the weldment surface to form two orthogonal red laser stripes, which can be captured by the camera. Because the weld lines are higher than the tower surface, there are convex shapes on the strips around the weld lines. When the CSL device is close to an intersection of a vertical and a horizontal weld line, two convex arcs will appear on the stripes in the captured images, according to the optical reflection principle. This characteristic is different to vision-based approach and enables us to detect single and cross weld lines even when the weld line and its background have similar color.

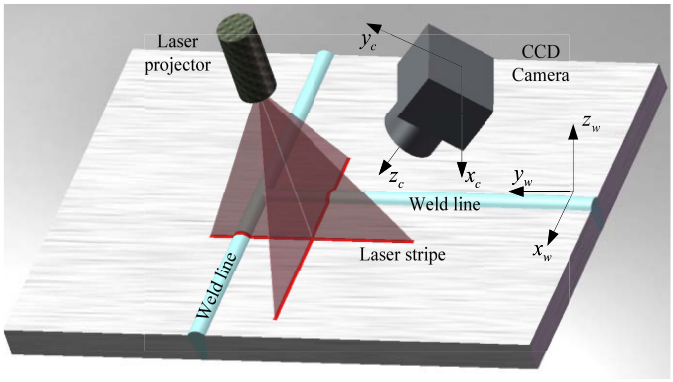

Fig. 3. Illustration of the CSL projector and the CCD camera on weld lines.

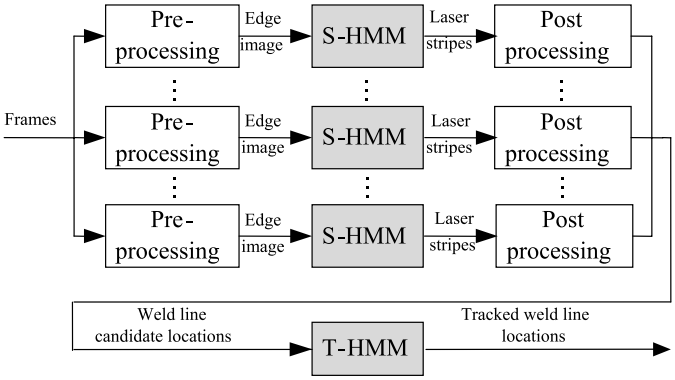

Fig. 4. Flowchart of the proposed weld line detection and tracking approach with STC-HMMs.

The CCD camera captures 20 color video frames in H.264 format with 640 × 480 pixel resolution per second. The video frames are transmitted to a PC with a wireless module for weld line detection and tracking. The operations of detection and tracking are performed on the PC. Detection and tracking results will be converted into the Cartesian space of robot end-effecter frame and then transmitted to the robot to control its movement with an integrated proportional-integral-derivative (PID) controller in the robot.

For camera calibration, we follow the approach proposed in [35] and [36]. The control module is performed with a PID controller, as described in [37]. In the remainder sections, we will concentrate on the approach of weld line detection and tracking given the captured video frames.

III. Weld Line Detection and Tracking

Fig. 4 shows the flowchart of the proposed approach, which includes the modules of image preprocessing, S-HMM-based weld line detection, postprocessing, and T-HMM-based tracking.

A. Image Preprocessing

Under the environment of high illumination, the laser stripe can be swamped by the environment noise, as shown in Fig. 5(a). It can be observed that the signal–noise ratio is very low, making it difficult to precisely locate laser stripes. Fig. 5(b)–(d) shows its intensity distribution maps in red, green, and blue components, respectively. Among these components, red component is observed to have the highest signal–noise ratio in our task and therefore is used for component detection.

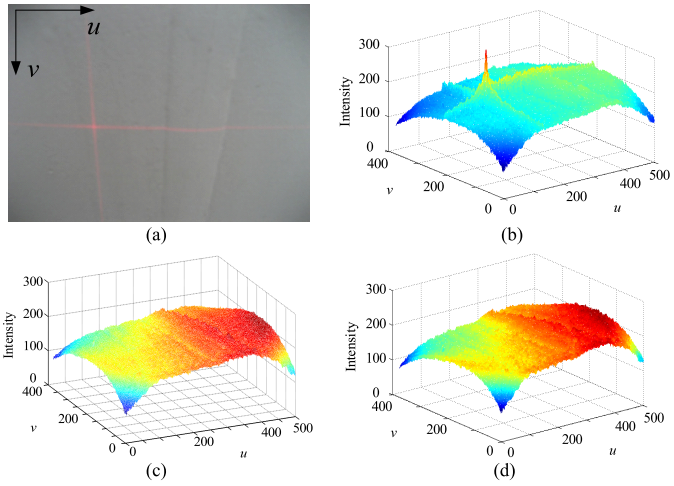

Fig. 5. Captured CSL image and its intensity distribution in red, green and blue color channels. (a) Captured image, where u and v are the column and row coordinates of the image, respectively, its intensity distribution of (b) red channel, (c) green channel, and (d) blue channel. It can be observed that the signal–noise ratio is the highest in red channel.

A histogram-based adaptive thresholding [38] approach is employed to convert red component images into binary images. After the thresholding operation, we can detect the stripe pixels by segmenting pixels with extreme values. Given the binary image of detected stripe pixels, a Canny edge detector [39] is used to extract the edge images, which will be the input observations of the S-HMMs, as shown in Fig. 6(a). The experiments show that the edge detection on color images can be affected by noise while the combination of histogram-based adaptive thresholding and edge detection on binary image is more robust.

B. Spatial HMM

In the vertical (v) or horizontal (u) direction of an edge image, each two adjacent edge pixels are defined as an edge pair. A stripe is made up of a sequence of edge pairs, as shown in Fig. 6(a). The distance of edge pairs on the stripe should be relatively small and the intensity of pixels between the edge pairs should be similar with each other. With this observation, center of mass [21] is used to detect the center point (peak of the laser strip) between each edge pair. Detected center points constitute the skeleton of the laser stripe.

Taking a horizontal stripe as an example, a center point at step t (tth column of the edge image) is described by a state $\omega_r(t)$, where r is the state index in the step t. All states, ω, are nonhomogeneous because the amount of center points is not equal in each step. The state can only be observed through a sequence of observed variables $V = \{v(1), \ldots, v(T)\}$.

Let $e_r(t), t = 1, \ldots, T, r = 1, \ldots, R(t)$ denote the coordinates of a column of edge pixels at step t. The center point between edge pair $(e_r(t), e_{r+1}(t))$ is defined as a state $\omega_r(t)$. $R(t)$ denotes the amount of center points at step t. $v_r(t) = |e_r(t) - e_{r+1}(t)|, t = 1, \ldots, T$, denoting the distance

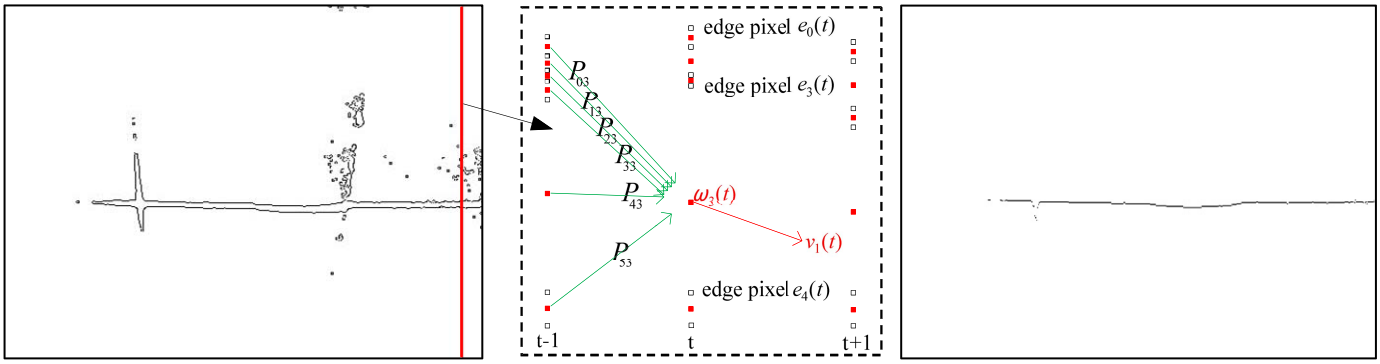

Fig. 6. Illustration of an S-HMM for stripe extraction. (a) Edge image and (b) illustration of the three steps of the S-HMM. The steps are from three columns of edge pixels of (a), where boxes represent edge pixels and square points represent center points of edge pairs, i.e., state ω of the S-HMM. P_{ij} is the transition probability from state i of step $t-1$ to state j of step t. (c) Extracted stripe skeleton.

between the edge pair $(e_r(t), e_{r+1}(t))$, is defined as an observation value of the S-HMM. If there is no edge point in a column, the column will be skipped. $m_r(t), t = 1, \ldots, T$, denoting the mean of the pixel intensity between edge pair $(e_r(t), e_{r+1}(t))$, is used to calculate the transition probability of the S-HMM. For example, $m_3(t)$ is the red component mean value of the image pixels between the edge pair $(e_3(t), e_4(t))$.

Given an observed sequence V, the function of S-HMM is used to choose a state sequence $\omega_r(t) = \{\omega_r(1), \ldots, \omega_r(T)\}$, $r = 1, \ldots, R(T)$, $t = 1, \ldots, T$, which is optimal in terms of defined observation and transition probability as

$$P(V) = \prod_{t=1}^{T} \sum_{r=1}^{R(t)} P\left(v_{\mathrm{r}}(t)|\omega_r(t)\right) P\left(\omega_r(t)|\omega_r(t-1)\right) \quad (1)$$

where $R(t)$ is the amount of hidden states of step t and T is the sequence length.

Given the above definitions, we can construct an S-HMM to detect the horizontal stripe. In the S-HMM, the initial state probability is set as

$$P\left(\omega(t=1)\right) = \frac{1}{R(1)}. \quad (2)$$

In the S-HMM, we define two observation states corresponding to locations of stripe and nonstripe, respectively. Therefore, the observation probability is defined as a Bernoulli distribution (zero–one distribution). The observed probability is defined as

$$P\left(v(t)|\omega(t)\right) = \begin{cases} 1.0, & \text{if } (v_r(t) \le H_e) \\ 0.0, & \text{otherwise} \end{cases} \quad (3)$$

where H_e is an empirically determined threshold, which is set to 10 pixels when the images have a size of 640 × 480 in pixels. By (3), we can see that if the distance between two adjacent edge pixels is larger than H_e, the observation probability reduces to zero, which is based on the fact that the width of the stripe is usually small in the image domain and the distance from the camera to the weldment surface is almost constant even when the robot is moving. When there is high lighting and/or noises, the laser stripes might be weak and thin. To avoid missing the observation states, we only set an upper threshold H_e without a lower threshold, although a lower threshold can enable the system to have a higher computation speed in ideal environments.

The transition probability is calculated from the spatial distance and intensity difference between states by

$$P(\omega_j(t)|\omega_i(t-1)) = \exp\left\{-(w_1, w_2) \cdot \left(\frac{d_{ij}^2}{\sigma_d^2}, \frac{f_{ij}^2}{\sigma_f^2}\right)'\right\}, \quad i, j \in [1, R(t)] \quad (4)$$

where d_{ij} is the spatial distance and f_{ij} is the intensity difference between the center points of two adjacent steps (two columns in the edge image) w_1 and w_2 are two weights to balance the importance of the spatial distance and the intensity difference where $w_1 + w_2 = 1.0$.

The distance from point i of step $t-1$ to point j of step t is defined as $d_{ij} = ((c_i(t-1) - c_j(t))^2 + 1)^{1/2}$, where $c_i(t-1)$ and $c_j(t)$ are the vertical coordinates (image row) of center point i at step $t-1$ and center point j at step t, respectively. $f_{ij} = \left|m_i(t-1) - m_j(t)\right|$ is defined as the difference between $m_i(t-1)$ of step $t-1$ and $m_j(t)$ of step t. σ_d^2 is the variance of distance, which can be calculated by

$$\sigma_d^2 = \frac{\sum_{t=1}^{T} \sum_{i,j=1}^{R(t)} \left[d_{ij}(t) - \overline{d}\right]^2}{\prod_{t=0}^{T} R(t)}, \quad i, j \in [1, \ldots, R(t)] \quad (5)$$

where $\overline{d}$ is the mean of d_{ij}. σ_f^2 is the variance of the intensity difference, which can be calculated by

$$\sigma_f^2 = \frac{\sum_{t=1}^{T} \sum_{i,j=1}^{R(t)} \left[f_{ij}(t) - \overline{f}\right]^2}{\prod_{t=1}^{T} R(t)}, \quad i, j \in [1, \ldots, R(t)] \quad (6)$$

where $\overline{f}$ is the mean of f_{ij}. w_1 and w_2 are weights, which could be learned from training data by the maximum likelihood estimation or the maximum *a posteriori* estimation.

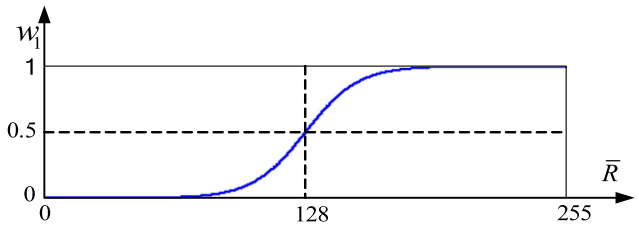

Fig. 7. Relationship between weight w_1 and the mean value of red component.

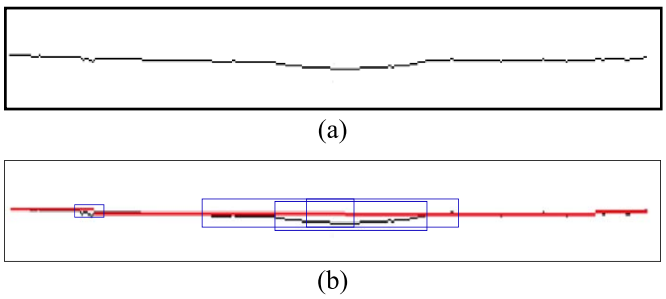

Fig. 8. (a) Stripe skeleton after filling the gap and (b) located weld line candidates on the stripe. Red line: the base line. Blue boxes: the sliding windows for weld line candidates.

In the experiments, it is found that w_1 and w_2 are mostly consistent with a hyperbolic tangent function, as shown in Fig. 7. Therefore, w_1 and w_2 can be calculated by

$$\begin{cases} w_1 = \frac{1+\tanh(\bar{R}-128)}{2} \\ w_2 = \frac{1-\tanh(\bar{R}-128)}{2} \end{cases} \quad (7)$$

where $\bar{R}$ is the mean intensity of the red channel of the captured image.

Given the above definitions, the problem of laser stripe extraction can be solved by maximizing (1), which is formulated as a dynamic programming problem, and could be solved using the Viterbi decoding algorithm [40]. After a Viterbi decoding procedure, an image of filtered stripe center points can be obtained as shown in Fig. 6(c). Befitting from the smooth function of S-HMM, it can be seen that noise pixels are filtered out and a clean skeleton of the laser stripe is obtained.

S-HMM is used to detect skeletons of horizontal laser stripes. Extracting skeletons of vertical laser stripes can be done in the same way. When detecting a horizontal stripe, the vertical stripe becomes noise and vice versa. The noise might cause false detections of center points, and therefore the detected stripe skeleton has a gap at the intersection of the vertical and horizontal stripes, as shown in Fig. 6(c). In the postprocessing, we fill the gap using a morphological close operation. A detected skeleton after the morphological operation is shown in Fig. 8(a).

C. Temporal HMM

On the extracted stripe, weld line locations can be determined by detecting the convex arc. We first use the Hough transform to detect the base line of stripe, as shown in Fig. 8(b). Then, we define the following measurement to locate weld line candidates on the extracted stripe:

$$M(w) = \frac{1}{|w| \cdot \sigma^2} \left(s(w) \cdot \sum_{t \in w} \left(P\left(\omega(t) | \omega(t-1)\right)\right)^{-1} \right) \quad (8)$$

where w denotes the current window with a width $|w|$, σ^2 is the variance of values of the distance from the points on the arc to the base line in the window, $s(w)$ is the area of the closed region between the convex arc and the base line (equal to the number of pixels in the region), and $P(\omega(t)|\omega(t-1))$ is the transition probability defined in (4). The larger the value of $M(w)$, the more likely the current window w compares with a weld line. When conducting the detection, we define two constraints to eliminate noise from detected area: 1) the region between the arc and the base line should be closed and 2) the area s should be larger than a predefined threshold (200 pixels) when the image has a size 640 $\times$ 480 in pixels.

Because weld line shapes might be irregular and could have bite side, weld tumor, or hollow, using the window of maximum measement value of (8) is not robust. Those windows, whose locations, areas, colors and widths are similar with to the weld line, should be considered. Therefore, when locating a weld line, a sliding window search is used over different window widths. The windows with local maximum $M(w)$ are detected as weld line candidates and fed to the T-HMM for weld line tracking, as shown Fig. 9(a).

In T successive frames, the weld line locations are assumed to form a state sequence $\{w_n(1), \ldots, w_n(T)\}$, where n is the index of the states in each time step corresponding to a candidate location of weld line on laser stripe at time step t and T is the time sequence length (number of the frames). At each time step t (the tth frame), there are $N(t)$ states $\{w_1(t), \ldots, w_{N(t)}(t)\}$ corresponding to $N(t)$ weld line candidates located using (8). $w_n(t)$ is nonhomogeneous. We can convert it into a homogeneous by inserting zeros to some steps, however, so that we have $N_{\max} = \max(N(t))$, $t = 1, \ldots, T$ states in each time step. The probability that the model produces a sequence V^T of visible states is described as follows:

$$P\left(V^T\right) = \sum_{n=1}^{N_{\max}} \prod_{t=1}^{T} P\left(v_n(t) | w_n(t)\right) P\left(w_n(t) | w_n(t-1)\right). \quad (9)$$

Similar to the S-HMM, the state probability is initialized as

$$P\left(w(t=1)\right) = \frac{1}{N(1)}. \quad (10)$$

As (3), in T-HMM, we also define two observation states, corresponding to locations of weld and nonweld lines. Therefore, the observation probability is defined as the Bernoulli distribution (zero–one distribution). The observation state corresponding to location of weld line is assigned the maximum observation probability 1.0. This introduces simpler implementation and lower complexity.

Let $\delta_{w_n}(t)$ denote the first left point of the window $w_n(t)$ at time step t, $|w_{t-1}|$ denote candidate window width and Δ_{t-1} be the first left point of the weld line at time step $t-1$.

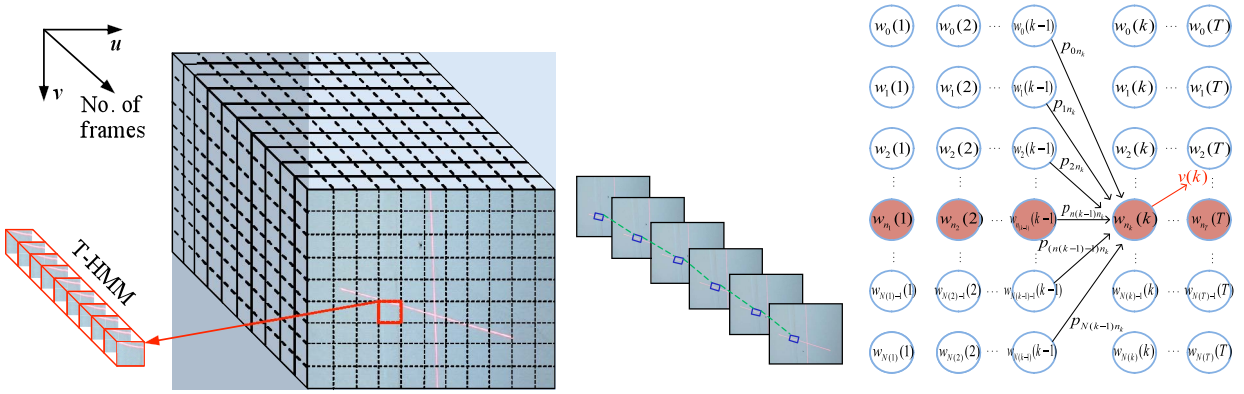

(a) (b) (c)

Fig. 9. T-HMM for weld line tracking. (a) Illustration of the T-HMM with detection results of Section III-B. (b) Weld line tracking process. (c) Illustration of steps of the T-HMM, where each state corresponds to a detected candidate weld line location. Filled circles: tracked weld line locations.

The observation probability can be defined as

$$P(v(t)|w(t)) = \begin{cases} 1.0, & \text{if } \Big(\big(H_{\min} < |w_n(t)| < H_{\max}\big) \\ & \quad \cap\Big(\Big(\Delta_{t-1} - \frac{|w_{t-1}|}{2}\Big) < \delta_{w_n}(t) \\ & \quad < \Big(\Delta_{t-1} + \frac{3|w_{t-1}|}{2}\Big)\Big)\Big) \\ 0.0, & \text{otherwise} \end{cases} \tag{11}$$

where $H_{\min}$ and $H_{\max}$ are empirically determined two thresholds of $w_n(t)$, which are equal to the width of the candidate weld line windows. If none of windows is classified as a weld line, i.e., $P(v(t)|w(t)) = 0.0$ at step t, the weld line location of the current frame is replaced by the weld line location of its previous frame.

The transition probability of the states $w_i(t-1)$ and $w_j(t)$ between adjacent frames is defined as

$$P\big(w_j(t)\,|w_i(t-1)\big) = \exp\left\{-\frac{1}{\mu \cdot s(t)}\left(\frac{d_l + d_r}{2}\right)(|s(t) - s(t-1)|)\right\} \tag{12}$$

where $s(t)$ describes the area of the closed region between the arc and the base line in frame t, as defined in (8). μ is a coefficient reflecting the importance of transition among the frames. Considering the robot's speed and direction, there is a difference between the transition probabilities of the horizontal and vertical laser stripes. (x_l, y_l) and (x_r, y_r) are the coordinates of left and right endpoints. In the laser stripe of the horizontal (u) direction, d_l and d_r are the Euclidean distance of the left and right endpoints of the two observation windows in the tth and $(t-1)$th frames as follows:

$$d_l = \sqrt{(x_l(t) - x_l(t-1))^2 + (y_l(t) - y_l(t-1))^2} \tag{13}$$

$$d_r = \sqrt{(x_r(t) - x_r(t-1))^2 + (y_r(t) - y_r(t-1))^2}. \tag{14}$$

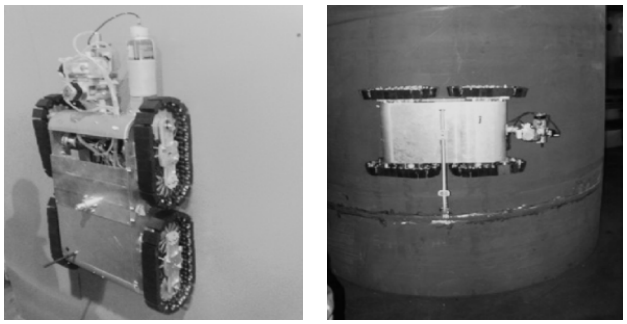

(a) (b)

Fig. 10. Wall climbing robot platform. The robot equipped with CSL device is moving in (a) vertical direction and (b) horizontal direction.

When defining the transition probability for the vertical (v) laser stripes, we need to consider the movement of the robot. The differences of the vertical windows between adjacent frames are defined in (15) and (16), which is shown at the bottom of this page, where $(x_{\text{top}}, y_{\text{top}})$ and $(x_{\text{btm}}, y_{\text{btm}})$ are the top and bottom points of windows in the vertical stripe, respectively, du and dv are the speeds of the robot in u and v directions, respectively, and τ is the interval between adjacent frames.

Given the above definitions, the problem of weld line tracking is solved by maximizing (9), which is also formulated as a dynamic programming problem and solved by a Viterbi decoding algorithm. After the Viterbi decoding procedure, tracked locations of weld lines in successive video frames are determined.

IV. Experiments

The proposed approach is tested in four video sequences captured from a mobile platform, as shown in Fig. 10.

$$d_{\text{top}} = \sqrt{\left(x_{\text{top}}(t) - \left(x_{\text{top}}(t-1) + \int_0^{\tau} du\right)\right)^2 + \left(y_{\text{top}}(t) - \left(y_{\text{top}}(t-1) + \int_0^{\tau} dv\right)\right)^2} \tag{15}$$

$$d_{\text{btm}} = \sqrt{\left(x_{\text{btm}}(t) - \left(x_{\text{btm}}(t-1) + \int_0^{\tau} du\right)\right)^2 + \left(y_{\text{btm}}(t) - \left(y_{\text{btm}}(t-1) + \int_0^{\tau} dv\right)\right)^2} \tag{16}$$

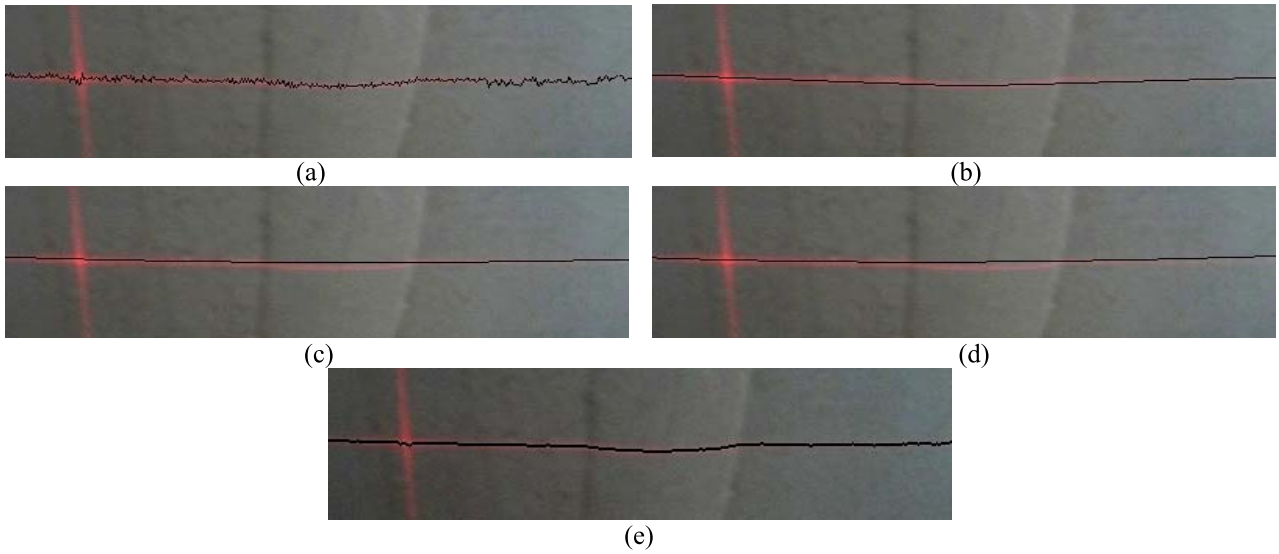

Fig. 11. Comparisons of laser stripe extraction results. (a) Results of Strobl's approach [12], (b) linear segments [9], (c) quadratic segments [9], (d) Akima splines [9], and (e) proposed S-HMM.

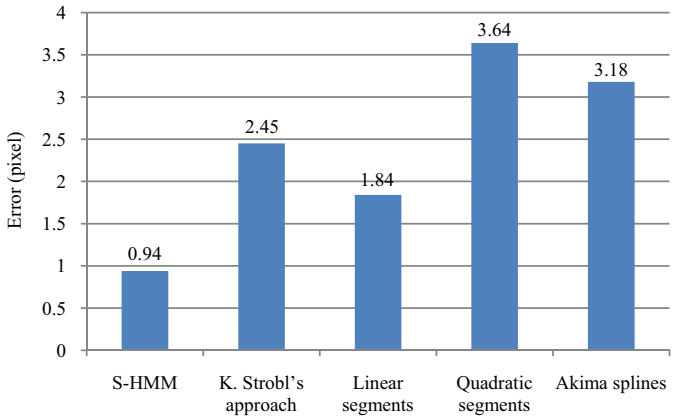

Fig. 12. Laser stripe extraction errors of five approaches.

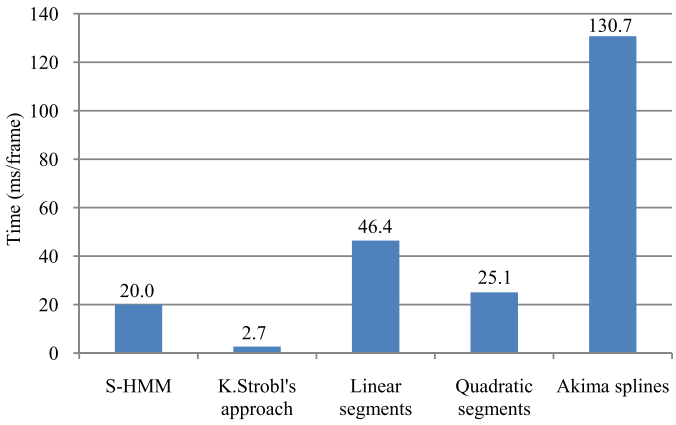

Fig. 13. Running time of five approaches.

The video sequences totally have 1000 frames with hand-marked ground truth. We use three experiments to evaluate the proposed approach and compare it with other approaches. These algorithms are implemented in C++ and are tested on an Intel Core i3-2130CPU of 3.4 GHz. In the CSL device, a 650-nm laser projector and a color camera of SONY 1/4-in CCD are used.

A. Stripe Extraction

In the laser stripe extraction, the proposed S-HMM-based approach is compared with the approaches in [9] and [12]. In [12], Strobl presents an approach of laser stripe extraction with Sobel edges. In [9], Usamentiaga *et al.* use linear segments, quadratic segments, and Akima splines, respectively, to extract laser stripes after a split-remove-fill procedure. Fig. 11 shows the laser stripe extraction results in the horizontal direction with the above methods and ours. It can be seen that the stripe detected by the proposed approach fits to the true stripe and weld line best. The most important thing is that the proposed approach can capture the very small weld line convex, which might be filtered out [Fig. 11(c) and (d)] in other approaches [Fig. 11(b)–(d)].

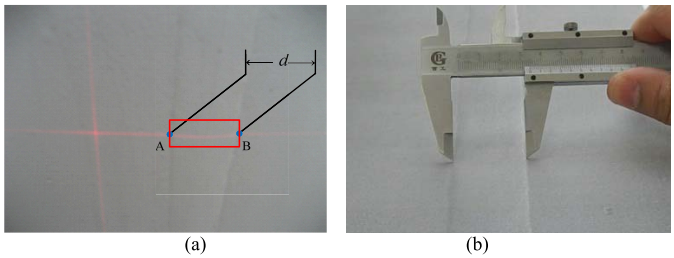

Fig. 14. Illustration of visual and mechanical measurement approaches. (a) Illustration of the endpoints A and B and measured weld width d in the tracking procedure. (b) Weld width measured with a vernier caliper.

To compare the effectiveness of the methods, we evaluate the stripe extraction errors of the five approaches. The extraction error is defined as the average pixel difference between stripes in ground-truth and automatic extraction results. It can be observed in Fig. 12 that the S-HMM has the highest accuracy. Compared with the second best approach (linear segments), our approach has a significant improvement, reducing the error from 1.84 to 0.94 pixels.

The average run time of stripe skeleton extraction is also compared, which is shown in Fig. 13. The proposed

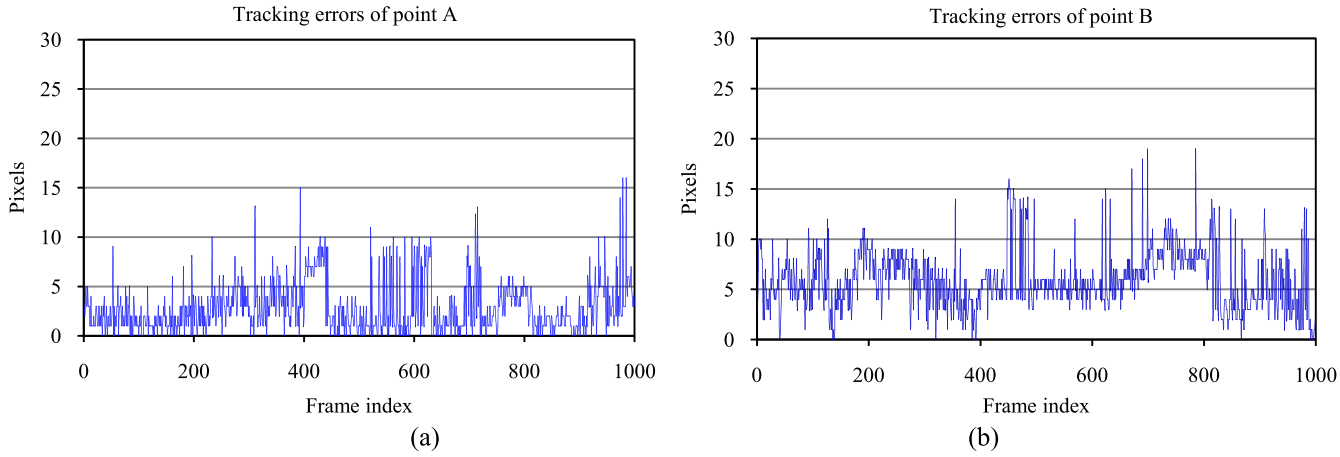

Fig. 15. Tracking errors measured by two endpoints (a) A and (b) B.

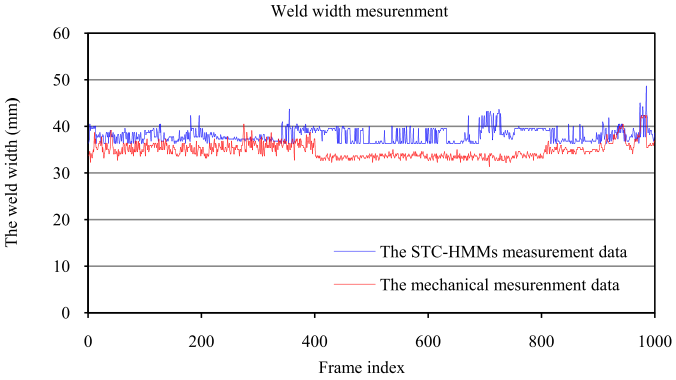

Fig. 16. Comparison of measured weld width by the STC-HMMs-based approach and mechanical measurement.

Fig. 17. Weld width measurement errors by the STC-HMMs. It can be observed that there are abrupt large errors in some frames. The errors reduce much after several frames.

S-HMM is slower than Strobl's approach and faster than the rest. In general, a processing speed with 20 ms/frame is fast enough for the practical applications. It implies that even the algorithm is ported to an embedded platform it can also have real-time performance.

B. Weld Line Tracking and Measurement

To evaluate the accuracy of the STC-HMMs method, we use the location error of the two endpoints (two intersections between a laser stripe and both weld toes of a weld line) as a measure. As shown in Fig. 14(a), two endpoints A and B corresponding to the intersection points between the weld toes and the laser stripe are defined. The tracking performance is evaluated on these two points separately, using Euclidean distance between the ground-truth points and the tracking results.

When tracking the weld line, random noise, such as illumination variation or surface defect of the weld line may introduce the new detection error. However, the STC-HMMs guarantee fast convergence of error. It can be observed in Fig. 15 that the maximum error of A and B points is 16.5 pixels (∼5.5 mm in the world coordinate system) and 19 pixels (∼6.5 mm in the world coordinate system), respectively. The errors have a little effect on the robot navigation. The tracking errors are absolute values between the tracking locations and the ground truth locations of point A or B. It can be seen on the curve that the tracking errors are random.

It can be observed in Fig. 15(a) and (b) that the tracking errors of point B are a little larger than that of point A. In the experimental setting, the right side of the weld line is closer to the image edge, thus it introduces radial distortion, and makes the intensity of laser stripe on point B is lower than that of point A. This implies that laser stripes at point B have a lower signal–noise ratio than that at point A, and therefore the tracking errors of point B are larger than that of point A.

The results of the weld width measurement are also used to evaluate the proposed approach. We calculated the distance d between points A and B, as shown in Fig. 14(a). Then, the distance d is transformed from the image coordinate system to the world coordinate system to obtain the weld width. In the same location of the weld line, we used a vernier caliper to measure the weld width, as shown in Fig. 14(b), for comparison. In Fig. 16, we compare the weld width measurement results by the STC-HMMs-based approach and mechanical measurement. The measurement errors of the two methods are shown in Fig. 17. In general, the average error, as shown by a polynomial fitting curve (the dashed curve) in Fig. 17, is much smaller than 7.5 mm, which is a tolerable

TABLE I
WELD WIDTH MEASUREMENT PERFORMANCE

Approach	Average width (mm)	Minimum error (mm)	Maximum error (mm)	Average error (mm)	Variance of errors (mm^2)	Localization error rate
Vernier caliper	34.8	--	--	--	--	--
S-HMM	40.8	0	49.8	6.0	11.4	14.0%
STC-HMMs	38.1	0	10.5	3.3	4.5	3.6%

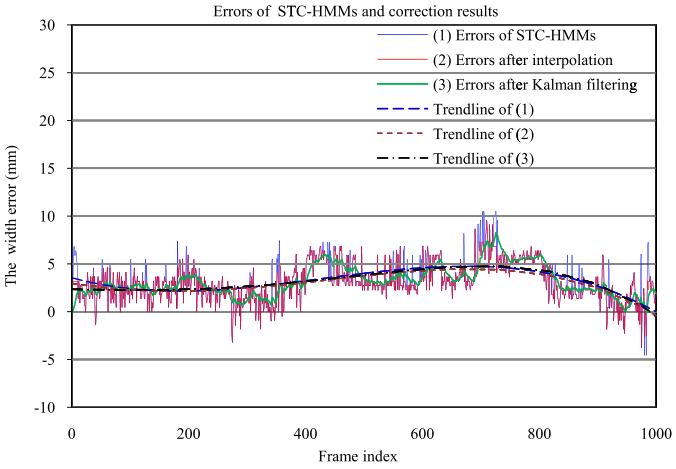

Fig. 18. Errors before and after correction.

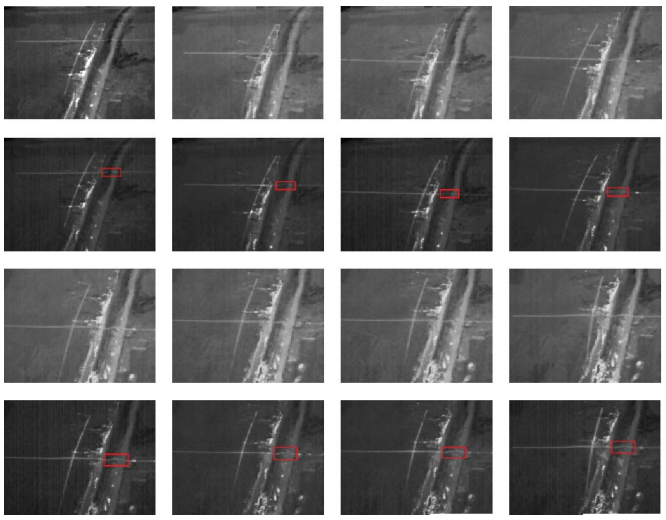

Fig. 19. Weld line tracking examples. First and third rows: frames containing high light and weld defects. Second and fourth rows: tracking results of the first and third rows, respectively.

error. It can be observed in Fig. 17 that there are small errors in most of the frames, which are introduced by environmental noise and the error of camera calibration.

A statistical analysis of minimum, maximum, average error, variance, and error rate is given in Table I. In our system, it is defined that if the width error value is larger than 7.5 mm

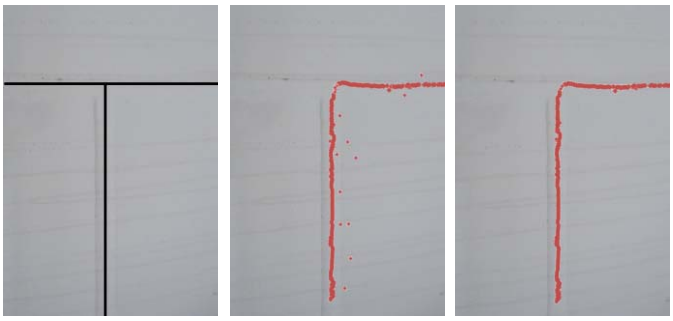

Fig. 20. (a) Center lines of two cross weld lines (ground truth). (b) Weld line tracking results with abrupt large errors. (c) Trajectory of the robot platform after the abrupt large errors are eliminated.

(the scanning range of the ultrasonic probe in our system), the localization result is considered as a false detection due to the scanning range of ultrasonic probe would not completely cover the weld line. The experiments in Fig. 17 involved 1000 frames, in which 36 frames' width errors are larger than 7.5 mm; therefore, the localization error rate is 3.6% When using the S-HMM for weld line detection without using the T-HMM, a window of maximum value of (8) is selected in one frame. It can be observed that the performance of weld line tracking is greatly improved after the temporal filtering. When using the measurement results of vernier caliper as the ground truth, the T-HMM reduces the average error of S-HMM from 6.0 to 3.3 mm, the variance of errors from 11.4 to 4.5 and the localization error rate from 14.0% to 3.6%. This performance meets the system requirement.

C. Elimination of Abrupt Large Errors

In Figs. 15 and 17, it is observed that there are abrupt large errors in some frames. We find that these abrupt large errors are due to the missing candidates in the video frames. In (11), two thresholds $H_{\min}$ and $H_{\max}$ are used to calculate the observation probability of the weld line windows. We empirically set 50% of the estimated weld linewidth to $H_{\min}$ and 200% of the estimated weld linewidth to $H_{\max}$. Due to the irregularity of the weld lines and illumination variation, the convex shapes of the weld lines in some frames can be very poor. Therefore, detected candidate windows can have width values out of the scope of $[H_{\min}, H_{\max}]$. In such conditions,

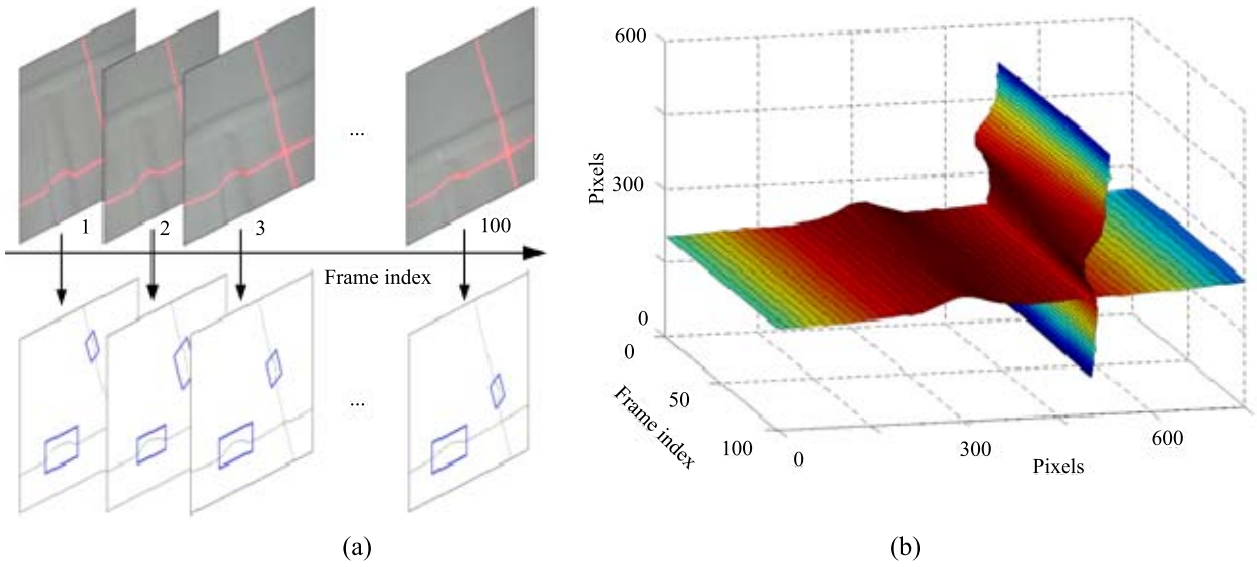

Fig. 21. (a) Images and weld line tracking results when the robot is moving toward a weld line intersection. (b) Weld locations and accumulated shapes in successive video frames.

false detection and tracking results are obtained, according to (9) and (12).

To reduce the abrupt large errors, we use an interpolation strategy. In practice, the weld line should be continuous and approximately straight. The speed of the wall climbing robot is ∼30 mm/s (∼1.5 mm/frame given a video frame rate of 20 fps). This shows that the change of stripe location should be very small between two successive frames. Therefore, when we cannot detect any candidate in a frame, we use the located weld line in the previous location as an estimation. This guarantees the smoothness of T-HMM and enables the approach to avoid abrupt large errors in most of the frames, as shown in Fig. 18. A Kalman filter [2] is also used to smooth the tracking results and eliminate abrupt errors. It can be observed that the smoothed results (Fig. 18, green curve) are slightly better than those based on the interpolation strategy. The using of Kalman filter introduces 52.7-ms delay in 1000 video frames. Although the time delay is negligible, the increasing of system complexity should not to be neglected.

In Fig. 19, we show some tracking results in video frames captured from a wild environment. Despite the high illumination and a large number of noises in these frames, our approach shows robust performance. In Fig. 20, we show the tracking results of cross weld lines. Although there are a few isolated tracking errors in Fig. 20(b), which shows some abrupt large errors, the robot platform can still move along the weld lines correctly. This further shows that the STC-HMMs are robust to errors and can track weld lines after the abrupt large errors are reduced with the proposed interpolation strategy.

Fig. 21(a) shows the weld line tracking results in 100 video frames. There are vertical and horizontal weld lines in the video sequence. It can be seen that the proposed approach detected both vertical and horizontal weld lines when the platform moved close to the intersection part of the two weld lines. The smooth shapes of detected and tracked weld line [the convex shapes in Fig. 21(b)] demonstrate the effectiveness of the proposed approach.

V. Conclusion

In this paper, we proposed an HMM and CSL-based weld line detection and tracking approach. The simple but effective CSL device provides an example for weld line measurement and we provide a general methodology, named STC-HMMs, for a kind of measurement problems in industrial applications.

The proposed S-HMM extracts laser stripe in horizontal and vertical orientations in each video frame and the T-HMM tracks weld line in a video sequence. In the S-HMM, a sliding window detection strategy is proposed to locate weld lines along skeletons of laser stripes. Proper observation and transition probability for both S- and T-HMMs are defined when detecting laser stripes and tracking weld line.

In video sequences from a practical moving inspection platform, we validated the effectiveness of the proposed approach through detecting single and cross weld lines. The experiments show that the S-HMM can extract laser stripes accurately and is demonstrably superior to the segmentation method based on the histogram. The T-HMM further improves the accuracy of weld line location in successive video frames. By combining features of color, location, area, and using continuity of weld lines, the proposed STC-HMMs show robustness over environment noises, illumination variance, and irregular platform motions. In addition, the robustness is obtained without losing the real-time performance.

Acknowledgment

The authors would like to thank D. Zhao from the Chinese Academy of Sciences, Beijing, China, Dr. Q. Qiu from Duke University, Durham, NC, USA, and Dr. G. Zhu from UC Berkeley, Berkeley, CA, USA, for their valuable discussions of this paper, and the editor and anonymous reviewers for their constructive comments.

REFERENCES

[1] E. Carvalho, L. Molina, E. Freire, R. Freire, and B. Luciano, "Fillet weld identification for automatic inspection of spherical tanks," in *Proc. IEEE Instrum. Meas. Technol. Conf.*, May 2007, pp. 1–6.

[2] E. Carvalho, B. Luciano, R. Freire, L. Molina, and E. Freire, "Fault-tolerant weld line detection for automatic inspection of storage tanks based on distance and visual information fusion," in *Proc. IEEE Instrum. Meas. Technol. Conf.*, May 2009, pp. 791–796.

[3] L. Molina, E. Carvalho, E. Freire, J. Montalvão-Filho, and F. Chagas, "A robotic vision system using a modified Hough transform to perform weld line detection on storage tanks," in *Proc. IEEE Latin Amer. Robot. Symp.*, Oct. 2008, pp. 45–50.

[4] L. Molina, R. Freire, E. Carvalho, and E. Freire, "A model-based fault-tolerant weld line detection for automatic inspection of storage tanks using visual information and α-β filter," in *Proc. Latin Amer. Robot. Symp. Intell. Robot. Meeting*, Oct. 2010, pp. 25–29.

[5] X. Wang, D. Liang, and T. Zhang, " A robust vision based weld center finding method in automatic ultrasonic nondestructive test," in *Proc. IEEE Int. Conf. Control Autom.*, May 2007, pp. 162–165.

[6] L. Zhang, J. Jiao, Q. Ye, Z. Han, and W. Yang, "Robust weld line detection with cross structured light and hidden Markov model," in *Proc. IEEE Int. Conf. Mech. Autom.*, Aug. 2012, pp. 1411–1416.

[7] Y. Gong, X. Dai, and X. Li, "Structured-light based joint recognition using bottom-up and top-down combined visual processing," in *Proc. Int. Conf. Image Anal. Signal Process.*, Apr. 2010, pp. 507–512.

[8] Y. Li, Y. F. Li, Q. Wang, D. Xu, and M. Tan, "Measurement and defect detection of the weld bead based on online vision inspection," *IEEE Trans. Instrum. Meas.*, vol. 5, no. 9, pp. 1841–1849, Jul. 2010.

[9] R. Usamentiaga, J. Molleda, and D. Garcia, "Fast and robust laser stripe extraction for 3D reconstruction in industrial environments," *Mach. Vis. Appl.*, vol. 23, no. 1, pp. 179–196, 2010.

[10] J. Molleda, R. Usamentiaga, F. Bulnes, J. Granda, and L. Ema, "Uncertainty propagation analysis in 3-D shape measurement using laser range finding," *IEEE Trans. Instrum. Meas.*, vol. 61, no. 5, pp. 1160–1172, May 2012.

[11] J. Molleda, R. Usamentiaga, D. Garcia, F. Bulnes, and L. Ema, "Shape Measurement of steel strips using a laser-based three-dimensional reconstruction technique," *IEEE Trans. Ind. Appl.*, vol. 47, no. 4, pp. 1536–1544, Jul./Aug. 2011.

[12] K. Strobl, W. Sepp, E. Wahl, T. Bodenmuller, M. Suppa, J. Seara, and G. Hirzinger, "The DLR multisensory hand-guided device: The laser stripe profiler," in *Proc. Int. Conf. Robot. Autom.*, Apr. 2004, pp. 1927–1932.

[13] J. Wu, J. Smith, and J. Lucas, "Weld bead placement system for multipass welding [using transputer-based laser triangulation vision system]," *IEE Proc., Sci., Meas. Technol.*, vol. 143, no. 2, pp. 85–90, Mar. 1996.

[14] R. White, J. Smith, and J. Lucas, "Vision-based gauge for online weld profile metrology," *IEE Proc., Sci., Meas. Technol.*, vol. 141, no. 6, pp. 521–526, Nov. 1994.

[15] T. Bodenmuller, "Streaming surface reconstruction from real-time 3D measurements," Ph.D. dissertation, Tech. Univ. Munchen, Munich, Germany, 2009.

[16] H. Asakura, A. Yamashita, and T. Kaneko, "3-D measurement of an object by a mobile robot equipped with a laser range finder," in *Proc. Joint Symp. Sister Univ. Mech. Eng.*, Aug. 2004, pp. 107–110.

[17] G. Fu, P. Corradi, A. Menciassi, and P. Dario, "An integrated triangulation laser scanner for obstacle detection of miniature mobile robots in indoor environment," *IEEE/ASME Trans. Mech.*, vol. 16, no. 4, pp. 778–783, Aug. 2011.

[18] O. Duran, K. Althoefer, and L. D. Seneviratne, "Automated pipe defect detection and categorization using camera/laser-based profiler and artificial neural network," *IEEE Trans. Autom. Sci. Eng.*, vol. 4, no. 1, pp. 118–126, Jan. 2007.

[19] G. Ho and J. Kim, "Model-based light stripe detection for indoor navigation," *Opt. Lasers Eng.*, vol. 47, no. 1, pp. 62–74, 2009.

[20] L. Lu, C. Ordonez, E. Collins, E. Coyle, and D. Palejiya, "Terrain surface classification with a control mode update rule using a 2D laser stripe-based structured light sensor," *Robot. Auto. Syst.*, vol. 59, no. 11, pp. 954–965, 2011.

[21] R. Fisher and D. Naidu, "A comparison of algorithms for subpixel peak detection," in *Image Technology: Advances in Image Processing, Multimedia and Machine Vision*. New York, NY, USA: Springer-Verlag, 1996, pp. 385–404.

[22] E. Trucco, R. Fisher, A. Fitzgibbon, and D. Naidu, "Calibration, data consistency and model acquisition with laser stripers," *Int. J. Comput. Integr. Manuf.*, vol. 11, no. 4, pp. 293–310, 1998.

[23] F. Blais and M. Rioux, "Real-time numerical peak detector," *Signal Process.*, vol. 11, no. 2, pp. 145–155, 1986.

[24] J. Forest, "New methods for triangulation-based Shape acquisition using laser scanners," Ph.D. dissertation, Univ. Girona, Girona, Spain, 2004.

[25] J. Forest, J. Salvi, E. Cabruja, and C. Pous, "Laser stripe peak detector for 3D scanners. a fir filter approach," in *Proc. Int. Conf. Pattern Recognit.*, Aug. 2004, pp. 646–649.

[26] J. Schnee and J. Futterlieb, "Laser line segmentation with dynamic line models," in *Proc. Comput. Anal. Images Patterns*, Aug. 2011, pp. 126–134.

[27] R. Ofner, P. O'Leary, and M. Leitner, "A collection of algorithms for the determination of construction points in the measurement of 3D geometries via light-sectioning," in *Proc. 2nd Workshop Eur. Sci. Ind. Collaborat.*, 1999, pp. 500–512.

[28] Y. Li, Q. Wang, Y. F. Li, D. Xu, and M. Tan, "On-line visual measurement and inspection of weld bead using structured light," in *Proc. IEEE Instrum. Meas. Technol. Conf.*, May 2008, pp. 2038–2043.

[29] Z. Fang, D. Xu, and M. Tan, "A vision-based self-tuning fuzzy controller for fillet weld seam tracking," *IEEE/ASME Trans. Mech.*, vol. 16, no. 3, pp. 540–550, Jun. 2011.

[30] A. Fernandez, R. Garcia, E. Alvarez, A. Campos, D. Garcia, R. Usamentiaga, M. Jimenez, and J. Garcia, "Low cost system for weld tracking based on artificial vision," in *Proc. IEEE Ind. Appl. Conf.*, Oct. 2009, pp. 1–8.

[31] Z. Xu and P. Ma, "A wall-climbing robot for labelling scale of oil tank's volume," *Robotica*, vol. 20, no. 2, pp. 209–212, 2002.

[32] W. Shen, J. Gu, and Y. Shen, "Proposed wall climbing robot with permanent magnetic tracks for inspecting oil tanks," in *Proc. IEEE Int. Conf. Mech. Autom.*, Jul./Aug. 2005, pp. 2072–2077.

[33] L. Kalra, W. Shen, and J. Gu, "A wall climbing robotic system for non destructive inspection of above ground tanks," in *Proc. IEEE Can. Conf. Electr. Comput. Eng.*, May 2006, pp. 402–405.

[34] L. Kalra, J. Guf, and M. Meng, "A wall climbing robot for oil tank inspection," in *Proc. IEEE Int. Conf. Robot. Biomimet.*, Dec. 2006, pp. 1523–1528.

[35] Z. Zhang, "A flexible new technique for camera calibration," *IEEE Trans. Pattern Anal. Mach. Intell.*, vol. 22, no. 11, pp. 1330–1334, Nov. 2000.

[36] Y. F. Li and S. Y. Chen, "Automatic recalibration of an active structured light vision system," *IEEE Trans. Robot. Autom.*, vol. 19, no. 2, pp. 259–268, Apr. 2003.

[37] D. Xu, L. Wang, Z. Tu, and M. Tan, "Hybrid visual servoing control for robotic arc welding based on structured light vision," *Acta Autom. Sinica*, vol. 31, no. 4, pp. 596–605, 2005.

[38] P. D. Wellner, "Adaptive thresholding for the digital desk," Rank Xerox Res. Centre, Cambridge, U.K., Tech. Rep. EPC-93-110, 1993.

[39] J. Canny, "A computational approach to edge detection," *IEEE Trans. Pattern Anal. Mach. Intell.*, vol. 8, no. 6, pp. 679–698, Nov. 1986.

[40] H. Lou, "Implementing the Viterbi algorithm," *IEEE Signal Process. Mag.*, vol. 12, no. 5, pp. 42–52, Sep. 1995.

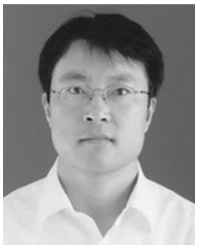

Liguo Zhang received the B.S. degree in automation from the University of Science and Technology Beijing, Beijing, China, in 2004. Since 2010, he has been pursuing the Ph.D. degree with the University of Chinese Academy of Sciences, Beijing.

His current research interests include robot vision, image processing, and pattern recognition.

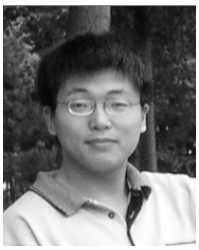

Qixiang Ye (M'10) received the B.S. and M.S. degrees in mechanical and electrical engineering from the Harbin Institute of Technology, Harbin, China, in 1999 and 2001, respectively, and the Ph.D. degree from the Institute of Computing Technology, Chinese Academy of Sciences, Beijing, China, in 2006.

He was an Assistant Professor from 2006 to 2009 and he has been an Associate Professor with the University of Chinese Academy of Sciences, Beijing, since 2009. He has been a Visiting Assistant Professor with the Institute of Advanced Computer Studies of the University of Maryland, College Park, since December 2012. He has published more than 50 papers in refereed conferences and journals. His current research interests include image processing, image based object detection and machine learning.

Dr. Ye pioneered the Kernel SVM based pyrolysis output prediction software which was put into practical application by SINOPEC in 2012. He developed two kinds of piecewise linear SVM methods which were successfully applied into image based object detection. He was a recipient of the Sony Outstanding Paper Award in 2005.

Wei Yang received the B.S. degree in electronic information engineering from PLA Information Engineering University, Zhengzhou, China, in 2010, and the M.S. degree from the University of Chinese Academy of Sciences, Beijing, China, in 2013.

His current research interests include pattern recognition and image processing.

Jianbin Jiao (M'10) received the B.S., M.S., and Ph.D. degrees in mechanical and electronic engineering from the Harbin Institute of Technology of China (HIT), Harbin, China, in 1989, 1992, and 1995, respectively.

He was an Associate Professor with HIT from 1997 to 2005. Since 2006, he has been a Professor with the Graduate University of Chinese Academy of Sciences, Beijing, China. His current research interests include image processing, pattern recognition, and intelligent surveillance.